Complete characterization of a plasma mirror for the production of high-contrast ultraintense laser pulses

G. Doumy, F. Quéré, O. Gobert, M. Perdrix, and Ph. Martin
Service des Photons, Atomes et Molécules, Commissariat à l'Energie Atomique, DSM/DRECAM, CEN Saclay, 91191 Gif sur Yvette, France

P. Audebert, J. C. Gauthier,* J.-P. Geindre, and T. Wittmann†
Laboratoire pour l'Utilisation des Lasers Intenses, Ecole Polytechnique, F91128 Palaiseau, France

(Received 26 June 2003; published 9 February 2004)

Improving the temporal contrast of ultrashort and ultraintense laser pulses is a major technical issue for high-field experiments. This can be achieved using a so-called ''plasma mirror.'' We present a detailed experimental and theoretical study of the plasma mirror that allows us to quantitatively assess the performances of this system. Our experimental results include time-resolved measurements of the plasma mirror reflectivity, and of the phase distortions it induces on the reflected beam. Using an antireflection coated plate as a target, an improvement of the contrast ratio by more than two orders of magnitude can be achieved with a single plasma mirror. We demonstrate that this system is very robust against changes in the pulse fluence and imperfections of the beam spatial profile, which is essential for applications.

DOI: 10.1103/PhysRevE.69.026402 PACS number(s): 52.38.−r

I. INTRODUCTION

Laser pulses of femtosecond (fs) to picosecond (ps) duration with very high peak powers (up to the PW) and extremely high intensities (up to 10^{21} W/cm^2) [1] are now available in many laboratories. Submitted to such intense light fields, almost any target gets rapidly ionized, and electrons in the resulting plasma oscillate at relativistic velocities. These light pulses therefore open the route to the experimental study of an extreme regime of laser-matter interaction [2], which has only been scarcely explored so far.

These ultrashort and ultraintense laser pulses are obtained with relatively small size subpicosecond laser systems thanks to the chirped pulse amplification (CPA) technique [3]. Two drawbacks of this technique are the presence of a temporal pedestal and of prepulses. The temporal pedestal has two origins: amplified spontaneous emission (ASE), which occurs on a nanosecond (ns) scale, and spectral clipping and residual aberrations of the spectral phase [4], giving rise to temporal structures on a sub-100 ps time scale. As for the prepulses, they are for instance due to the imperfect contrast of some of the optical elements (e.g., Pockel's cell-polarizers combinations) used in this type of laser. In this paper, the temporal contrast at time t is defined as the ratio of the peak intensity of the main laser pulse, and the intensity of the background (pedestal or prepulses) at this time t.

For a number of ultrahigh intensity experiments, it is of prime importance to use very high contrast, prepulse-free laser pulses. This is particularly true for experiments involving laser-solid interaction. For a peak intensity of 10^{18} W/cm^2 at the fundamental frequency of the laser, the energy contained in the pedestal or prepulses at the output of a typical high-power laser is generally high enough to generate a low-density plasma at the surface of a solid target, well before the main pulse. Then, because of the hydrodynamic expansion of this preplasma, the main pulse will not interact with a steep density-gradient solid target. This impedes the study of numerous exciting high-intensity laser-solid interaction processes, such as relativistic harmonics generation on solid surfaces [5], or Brunel absorption [6,7].

Increasing the peak intensity requires a parallel increase of the temporal contrast, so that prepulses and ASE remain at the same intensity level. Consequently, there has been intense research to increase the temporal contrast. This can be achieved either by improving the laser chain, or by cleaning the ultrashort pulse from its pedestal and prepulses at the end of the chain. The main methods studied so far are as follows:

(1) Electro-optic methods, which can remove ns prepulses for systems with a regenerative amplifier [8]; (2) methods based on nonlinear optical processes, such as frequency doubling at the output of the laser [9], clean pulse injection [10], nonlinear Sagnac interferometer [11], optical parametric CPA [12]; (3) self-induced plasma shuttering, also called plasma mirror (PM) [12–17].

In this work, we focus on the self-induced plasma shuttering method. The principle of plasma mirrors is the following. A laser beam is focused on a low-reflectivity vacuum-dielectric interface, so that most of the pedestal and prepulse energy is transmitted. As the intensity increases in time, electrons are excited in the dielectric medium by nonlinear mechanisms such as multiphoton absorption. The medium therefore acquires a ''metallic'' character. If the electron density exceeds the critical density at the laser wavelength (2×10^{21} cm^{-3} at 800 nm), the reflectivity suddenly increases: the plasma mirror is ''triggered,'' and the laser beam is reflected. For a proper choice of the incident fluence on the PM, triggering only occurs at the very beginning of the main pulse, and the reflected beam thus has an improved contrast ratio.

If the fluence is too high, triggering might occur too early, and the pedestal and prepulses will also be partly reflected.

*Present address: CELIA, Université Bordeaux I, 33405 Talence, France.

†Also at Department of Optics and Quantum Electronics, University of Szeged, Szeged, Hungary.

Moreover, with such an early triggering, the motion of the PM surface before and during the main pulse might distort the laser beam wave front, and thus prevent a good subsequent focusing. If the fluence is too low, triggering might occur too late or not occur at all. Therefore, the incident fluence is the most crucial parameter to make an efficient PM.

The first demonstration of an increase in the contrast ratio of a subpicosecond laser with a PM was given in Ref. [12]. A maximum reflectivity of about 50% and a tenfold improvement of the contrast ratio were obtained using a bulk dielectric plate. The authors underlined that the use of an antireflection coating on the dielectric plate would increase the contrast even more. A PM using a liquid jet, which allows to extend the method to high repetition rates, was implemented for the first time in Ref. [14]. The authors studied the reflectivity and contrast enhancement as a function of the incidence angle, polarization, and peak intensity. The highest contrast enhancement with a single PM, by a factor of 500, was reported in Ref. [15], which also emphasized the spatial filtering effect of the PM. A high-dynamic-range autocorrelation of the pulse after the PM provided the first direct evidence of the suppression of the pedestal. No strong distortion of the beam spatial profile was observed for the fluences used.

This paper presents the first detailed experimental and theoretical study of the PM. This study provides all the parameters required to design an efficient plasma mirror system, matched to the characteristics of a given high-intensity laser system.

The experimental study of the PM consisted in measuring the following quantities.

(1) Space and time-integrated reflectivities, using energy meters.

(2) Time-integrated reflectivities with spatial resolution, obtained by imaging the PM surface.

(3) Time- and space-resolved reflectivities. This was done by applying a chirp on the incident pulse. Measuring the spectrum of the reflected pulse then provides its temporal profile in a single shot. This provides a direct evidence of pedestal suppression with a PM, and also gives the turn-on time of the PM.

(4) Distortion of the beam spatial profile in the far-field (PM surface) and the near-field. This was, respectively, achieved by imaging the beam in the plane of the PM surface, and some distance after the PM. The near-field measurements provide qualitative information on the wave-front distortion induced in the PM plane.

(5) Time- and space-resolved position of the PM surface with $\lambda/50$ (16-nm) longitudinal resolution. This was again obtained in a single shot with a chirped incident pulse, by measuring its spectral phase after the PM using spectral-phase interferometry. This provides the time-resolved wave-front distortion induced by the PM.

All these measurements were performed on two types of targets, a bulk dielectric sample (quartz, 10% initial reflectivity in our experimental conditions) and an antireflection coating (less than 0.3% initial reflectivity), for different fluences above the PM triggering threshold. All the presented results are for an *S*-polarized incident beam, with an incidence angle of 45. We have found that the PM gives lower absolute reflectivities with *P*-polarized waves. This is probably due to resonant absorption [18] that occurs for *P*-polarized waves when the critical density is reached.

The theoretical study consisted in calculating the space- and time-dependent electric field and excitation density in the target, and the resulting instantaneous reflectivity. This was done by solving a one-dimensional (1D) Helmholtz equation [19], coupled with a nonlinear population equation describing the ionization of the dielectric target by the incident laser pulse. To simulate the results obtained at the highest intensities, the FILM code [20] was used to study the hydrodynamic expansion of the plasma on a sub-ps time scale.

We describe the experimental setup in Sec. II, and present the experimental results in Sec. III. The two models used in the simulations are described in Sec. IV. Section V is a detailed discussion of the performances of the PM. All fluences given in this paper correspond to the value at the center of the focal spot.

II. EXPERIMENTAL SETUP

The experiment was performed on the LUCA laser, at Saclay Laser Interaction Center. This is a high-power Ti-sapphire laser based on the CPA technique. A Kerr-lens mode-locked Ti-Sapphire oscillator generates a pulse train of 40 nm spectral width. These pulses are temporally stretched to about 300 ps before being amplified in a Ti-sapphire regenerative amplifier, followed by two four-pass amplifiers. After recompression, the energy per pulse is 100 mJ, and the pulse duration is 60 fs with a central wavelength of 800 nm. A few millijoules only were used in this experiment.

LUCA's contrast has been measured with a third-order cross correlator, and is $\approx 10^6$ one nanosecond before the main pulse, and reaches $\approx 10^4$ two picoseconds before the main pulse. The maximum peak intensity used in all measurements was of the order of a few 10^{15} W/cm^2, leading to maximum pedestal intensities of a few 10^{11} W/cm^2 on a ps time scale, and a few 10^9 W/cm^2 on a ns time scale. This is below the single-shot damage thresholds of dielectrics [21,22]. This suggests that in all our measurements, it was the main pulse, and not the pedestal, that triggered the PM. This is consistent with the fact that, when the oscillator was switched off, the ASE alone did not produce any damage at the target's surface even for multiple-shot exposition.

The experimental setup is shown in Fig. 1. The laser beam is separated into two parts (BS1): the main beam which reflects on the target (T), and a low-flux reference beam. To have the same configurations along the two paths, both the main and reference beams are focused (L1 and L3) and then imaged (L2 and L4), with a similar overall magnification factor. Special care was taken in the design of this experiment to avoid any nonlinearity in the transport of these beams, especially in the lenses and in the windows of the chamber. The main beam, of 18-mm top-hat aperture, is focused on the target with a long focal length MgF_2 lens (L1, $f=1200$ mm), chosen for its low nonlinear refractive index.

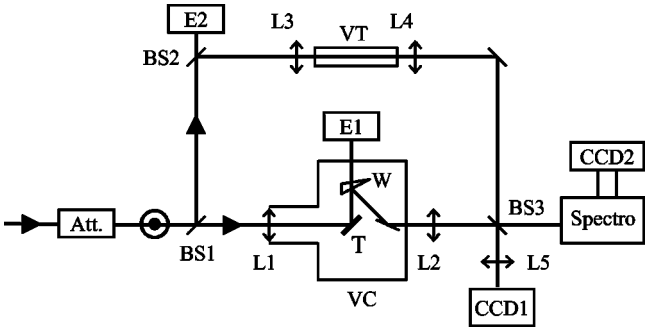

FIG. 1. Experimental setup. Att. stands for beam attenuator, BS for beam splitter, L for lens, T for target, W for wedge, E for energy meter, VC for vacuum chamber, and VT for vacuum tube. L5 was only set when the beam was imaged some distance after the PM surface.

After reflection on the target, a reflection on a wedge (W) is used to reduce the energy going through the output window. The part of the beam transmitted through the wedge is collected in a single-shot calorimeter (E1). The incident energy was simultaneously deduced from the measurement of a leak (BS2) in the reference beam with an identical calorimeter (E2). After proper calibration, the ratio of the reflected and incident energies provides the absolute space- and time-integrated reflectivity.

Both beams were imaged (lenses L2 and L4) on a high-dynamic charge coupled device (CCD) camera (CCD1). The focus of L2 was adjusted to image the target surface. The main beam image then gives access to a space-resolved relative reflectivity, and can also be used to calculate a space-integrated reflectivity. Given the magnification of this imaging setup and the CDD pixel size, a pixel corresponds to 3 μm in the object plane. The f number of L2 was $f/12$, leading to a spatial resolution of ≈ 12 μm. The full width at half maximum (FWHM) of the focal spot on the target measured with this system was 30 μm.

A second lens (L5) could be inserted in addition to L2, to image a plane located 60 cm after the target. In this configuration, comparing the images obtained at low and high intensities enabled to determine the distortion induced by the PM on the near-field beam spatial profile.

Both beams are simultaneously (BS3) imaged on the entrance slit of an imaging spectrometer (800 lines/mm, 1 m focal length).

If the two beams are separated spatially along the slit, this enables to compare their spectra, and measure in a single shot the effect of the PM on the main beam spectrum.

Superimposing the two beams spatially on the slit enables spectral interferometry measurements. This technique is based on the fact that two pulses, separated by a delay τ, interfere when they are sent in a spectrometer where dispersion is larger than the inverse of the delay. We typically used delays of a few ps between the two pulses. This is much larger than the coherence time of both beams. In this case, the relative spectral phase of the two pulses can be exactly extracted from the spectral interferogram fringe pattern using the mathematical treatment described in Ref. [23]. The effect of the PM on the main beam spectral phase is obtained by comparison with a low-energy shot, where the PM does not trigger.

All these measurements have been carried out both on near Fourier-limited pulses (60 fs duration) and on pulses chirped up to 4 ps. This chirp was introduced by setting the distance between the two gratings of the compressor so that the pulse is not recompressed to its Fourier limit. In this way, a quadratic spectral phase (linear chirp) remains on both the main and reference beams after compression.

Measurements using chirped pulses have two interests. First, we can see how the PM performs for longer (ps) pulses. But most interestingly, chirping the pulses makes it possible to follow in time the triggering and possible distortion of the PM in a single shot [24,25]. Indeed, for a pulse with a large chirp (duration large compared to the Fourier limit), there is a one-to-one mapping between time and frequency: each frequency corresponds to an arrival time on the target. To recover the temporal information and have access in a single shot to the behavior of the PM during the whole pulse duration, we only need to perform spectral measurements. The ultimate temporal resolution is the inverse of the spectral bandwidth of the pulse [25]. Typically, pulses have been chirped up to 4 ps and the temporal resolution is of the order of 60 fs.

Again, for measurements with chirped pulses, the main beam and the reference beam can either be spatially separated or superimposed on the spectrometer entrance slit. In the first case, comparing the spectra of the two beams provides the time-dependent reflectivity of the PM. In the second case, interferences between the two spectra, and comparison with a low-intensity reference shot, provide the change of spectral phase induced by the PM on the main beam. As we will see later, this change in spectral phase $\Delta\varphi(\omega(t))$ gives access to the change in position $\Delta z(t)$ of the PM surface, via $\Delta\varphi(\omega(t))=4\pi\cos(\pi/4)\Delta z(t)/\lambda$. The resolution on the spectral phase was limited by noise and was measured to be of the order of 0.1 rad: this corresponds to a $\approx\lambda/50$ (16-nm) resolution on the PM surface position.

III. EXPERIMENTAL RESULTS

A. Time-integrated reflectivities on quartz and antireflection coatings

Figure 2 shows the time-integrated reflectivity, measured at the center of the focal spot on the PM (i.e., the peak reflectivity), as a function of the fluence of a 60 fs pulse, in the case of quartz and of an antireflection coated dielectric plate.

In the case of quartz, below 5 J/cm^2, the reflectivity is equal to 10%, which is indeed the expected reflectivity for quartz for *S*-polarized 800 nm light at 45 incidence. Above this threshold fluence, the reflectivity increases continuously up to about 70% at 50 J/cm^2. Note that the optical breakdown threshold of quartz at this pulse duration is a few J/cm^2 [21,22,26]. This shows that this PM is a single-shot system. A fresh part of the target is required for each laser shot.

In the case of an antireflection coated dielectric plate, the initial reflectivity is less than 0.3%, while the high-fluence reflectivity is almost the same as for quartz. Thus, the con-

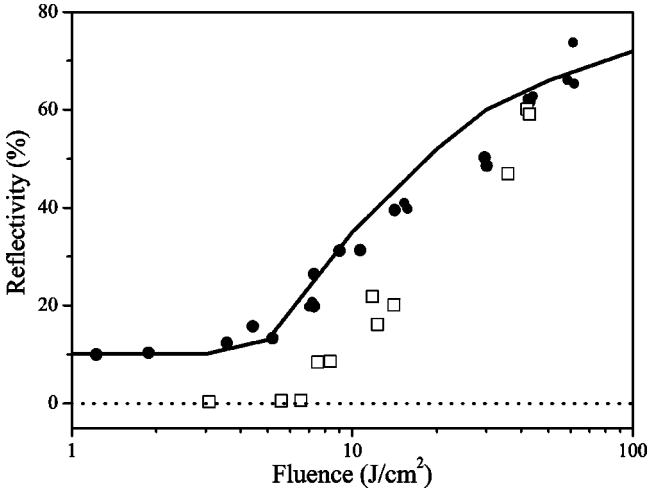

FIG. 2. Peak reflectivity of quartz (full dots) and antireflection coating (hollow squares), for a 60 fs incident pulse, as a function of the incident fluence. Note that with this linear *y* scale, the reflectivity of the antireflection coating at low fluence appears as ≈ 0. Full line: theoretical curve obtained from the population-propagation model.

trast between the high-fluence and low-fluence reflectivities is increased by more than one order of magnitude on this kind of target: as can be seen in Fig. 2, this ratio can reach several hundreds. The fluence at which this PM triggers is almost the same as for quartz. Note that the two reflectivity curves for quartz and the antireflection coating are indeed expected to merge at high fluence: once the plasma gets overdense near the surface, the field only penetrates the target over the skin depth and no longer sees the multiple layers of the antireflection coating.

Figure 3 shows the time- and space-integrated reflectivity (i.e., the overall reflectivity) as a function of the incident fluence, for a 60 fs laser pulse, measured on a bulk quartz sample. Because of the spatial averaging, the overall reflectivity is slightly lower than the peak reflectivity once the PM

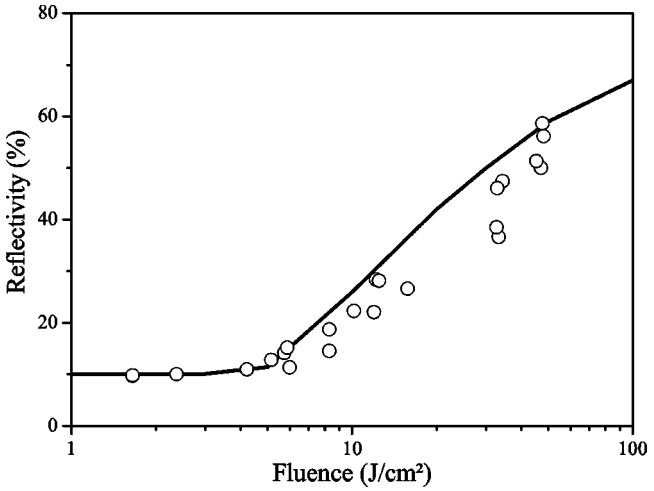

FIG. 3. Overall reflectivity of bulk quartz for a 60 fs incident pulse, as a function of the incident fluence. The full line shows the theoretical curve obtained from the population-propagation model.

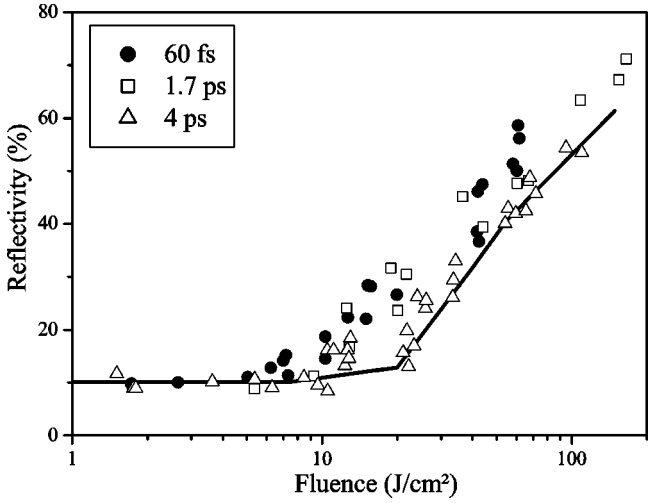

FIG. 4. Overall reflectivity for bulk quartz as a function of the incident fluence, for three different pulse durations. The full line shows the theoretical curve obtained from the population-propagation model for a 4 ps pulse.

triggers. This reflects a decrease of the PM reflectivity with the distance from the center of the focal spot.

Figure 4 shows the overall reflectivity measured for three pulse durations, 60 fs, 1.7 ps, and 4 ps, for a bulk quartz target. In this duration range, we see that the threshold fluence hardly varies with the pulse duration: this clearly indicates that the relevant factor for PM triggering is the incident fluence, and not the incident intensity. A similar behavior has been reported for optical breakdown thresholds of dielectrics [21,22].

B. Beam profiles

Figure 5 shows some cross sections of the main beam intensity profile (60 fs pulse duration) in two different planes: the surface of the target [far field, Figs. 5(a) and 5(b)], and a plane located 60 cm after the target [near-field, Figs. 5(c) and 5(d)]. Two sets of measurements are shown. In the upper panels, the incident fluence was too low for the PM to trigger, while in the lower panels, the incident fluence was 20 J/cm^2, and the PM triggered, as can be checked in Fig. 2.

Comparing the curves in Figs. 5(a) and 5(b) directly shows the effect of the PM on beam intensity profile, while comparing the curves in Figs. 5(c) and 5(d) gives some information on the wave-front distortion induced by the PM. However, this comparison can only be qualitative: for experimental reasons, the laser beam diameter on lens L1 was different for the low- and high-fluence shots.

The low-fluence far-field curve [Fig. 5(a)] shows that the incident beam profile on the target is close to an Airy function. This is the Fourier transform of the top-hat profile of the beam arriving on lens L1. The first Airy ring is clearly visible. On the low-fluence near-field curve [Fig. 5(c)], we observe that as the beam diverges from the target, it progressively recovers its top-hat shape, as expected.

At high fluence, the reflected beam profile in the target plane is still very smooth and clean. The first Airy ring is removed, its intensity being too low to trigger the mirror.

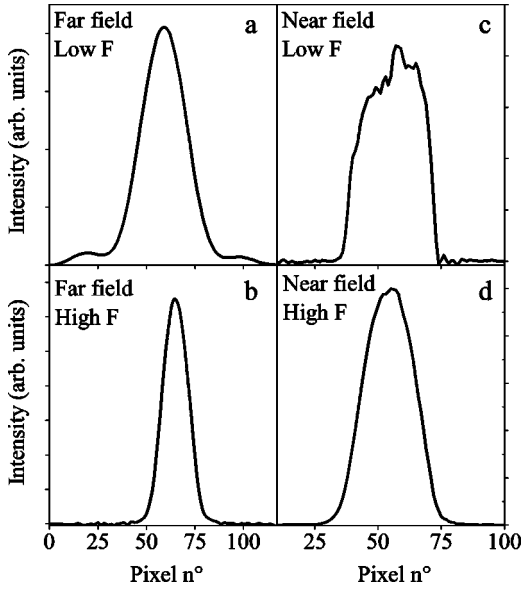

FIG. 5. Spatial profiles of the laser beam (60 fs pulse duration), at the surface of the target (a,b) and 60 cm after the target (c,d). The upper panels correspond to low-fluence shots, where the PM does not trigger, whereas the lower panels are high-fluence shots, where the PM triggered.

This shows that the PM acts as a low-pass spatial filter in the Fourier plane of lens L1.

This filtering effect leads to a smoothing of the sharp edges of the beam in the near field, as can be seen by comparing the low- and high-fluence profiles. These near-field curves also suggest that at this fluence, the PM does not induce a significant distortion of the wave front for a 60 fs pulse. A more accurate and quantitative characterization of the effect of the PM on the wavefront is provided by the interferometric measurements presented below (see Sec. III D).

C. Temporal dynamics of the reflectivity on an antireflection coating

Figure 6 shows the spectrum of the reflected beam, measured at the center of the focal spot, for a laser pulse chirped to 1.1 ps (i.e., 18 times its Fourier limit), for different incident fluences. The frequency scale has been converted into a time scale using the relationship $\omega(t)=t/\phi''+\omega_0$ between instantaneous frequency $\omega(t)$ and time t, where ω_0 is the central frequency and ϕ'' is the group delay dispersion ($\phi''=2.4\times10^4$ fs^2 in this case). This relationship is only valid for sufficiently high chirps. For such pulses, the spectrum directly provides the temporal profile of the pulse.

The triggering of the PM is observed to appear earlier in the pulse as the intensity increases: the higher the intensity, the faster the critical density is reached. The time-averaged reflectivity, which is proportional to the area under the curve, is also seen to increase with the incident fluence.

On the lowest-fluence curves (e.g., 5.4 J/cm^2), the PM is clearly observed to trigger significantly later than the maximum of the incident pulse, i.e., in the falling edge of the pulse. This would not be possible if multiphoton absorption

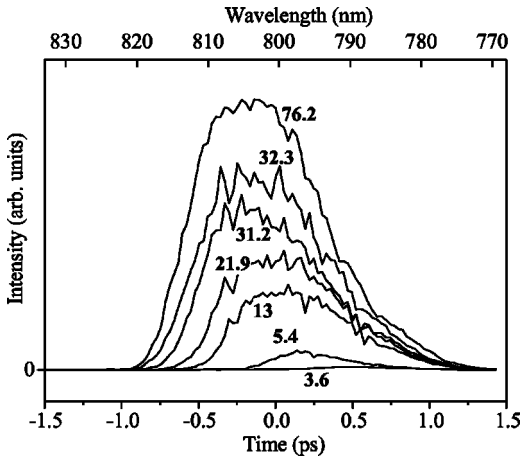

FIG. 6. Spectra of a pulse chirped to 1.1 ps, after reflection on a PM consisting of an antireflection coated plate target, for different incident fluences. The number on each curve indicates the corresponding incident fluence in J/cm^2. These spectra have been normalized by the incident fluence. The time scale has been obtained using the linear relationship between time and frequency for a linearly chirped pulse.

(or tunneling ionization) was the only mechanism involved in the generation of conduction electrons, since the efficiency of such a mechanism quickly falls off after the maximum of the pulse. On the opposite, the electronic avalanche mechanism can explain this observation, since its efficiency increases with the conduction electron density, and varies more gently with the laser field intensity. As we will see, the electronic avalanche mechanism indeed plays an important role in the triggering of the PM.

These curves also clearly show that in the fluence range that we have used, it is indeed the main pulse, and not the pedestal or a prepulse, that triggers the PM. Since we are dealing with an antireflection coating, the reflectivity before the main pulse is of the order of 0.3%, while we know from time-integrated measurements (Fig. 2) that the reflectivity reaches several tens of percent once the mirror is triggered. This implies that the PM improves the contrast by more than two orders of magnitude. In other words, these temporal profiles together with the reflectivity measurements provide a direct evidence of the efficient reduction of the pedestal.

D. Motion of the plasma mirror surface and wave-front distortion

Figure 7 shows a typical spectral interferogram obtained with a pulse chirped to 4 ps, with a fluence of about 140 J/cm^2. The horizontal axis corresponds to the wavelength scale and the vertical axis is the position along the spectrometer's slit. The fringe shift can easily be observed and is particularly strong in the center of the beam.

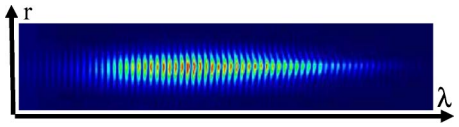

FIG. 7. Typical spectral interferogram for pulses chirped to 4 ps.

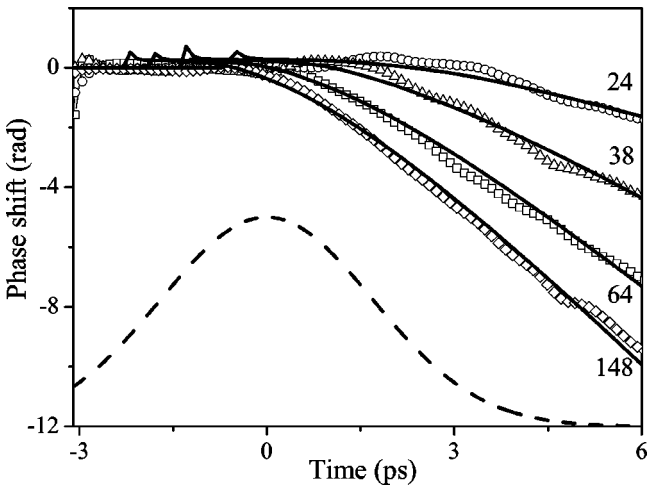

FIG. 8. Measured spectral phase of a pulse chirped to 4 ps, after reflection on the PM, for different incident fluences (hollow symbols). The number on each curve indicates the corresponding fluence in J/cm^2. The lines are theoretical fits obtained with the hydrodynamic code. The time scale was obtained as in Fig. 6, and the incident pulse temporal shape is shown in dashed line as a reference.

This interferogram gives access to the spatially resolved relative spectral phase $\varphi(\omega)$ of the main and reference beam. By subtracting the relative spectral phase $\varphi_0(\omega)$ measured for a low-fluence shot, we obtain the change in spectral phase $\Delta\varphi(\omega)$ induced on the main beam by the PM.

As before, since there is a one-to-one correspondence between time and frequency for such chirped pulses, this measured spectral phase actually is a temporal phase, via the relationship $\Delta\varphi(\omega)=\Delta\varphi(t/\phi''+\omega_0)$ ($\phi''\approx 8.7\times 10^4$ fs^2 for a 4 ps pulse).

There are two possible ways the PM can affect the temporal phase of the main beam: (1) the phase of the PM complex reflection coefficient r varies in time; (2) the surface of the PM moves, thus changing the optical path length of the main beam. Our calculations of the complex reflection coefficient, presented in Sec. IV, show that its phase does not vary by more than π, and that this variation only occurs when the electron density is close to the critical density. For most incident fluences, this only occurs in a narrow time interval. This leaves the motion of the PM surface as the main source of phase shift. The experimental accuracy on $\Delta\varphi(t)$ is about 0.1 rad. As already shown in Sec. II, this gives an accuracy of the order of $\lambda/50$ (16 nm) on the position of the PM surface.

Figure 8 shows the measured temporal phase $\Delta\varphi(t)$ for different incident fluences of a 4 ps pulse. $\Delta\varphi(t)$ is 0 until the PM triggers. It then presents a linear behavior, with a slope that increases as the fluence grows. This is characteristic of a plasma expansion in vacuum, as we will see in Sec. IV. The slope is determined by the velocity of the expansion, which is in a first approximation equal to the ion acoustic velocity. This velocity increases with the ionic temperature, and hence with the incident fluence.

The dependence of $\Delta\varphi(t)$ on the incident fluence implies that the induced phase shift is not homogeneous across the focal spot. In other words, the PM surface gets curved. Furthermore, this curvature varies in time. This possible distortion of the wave front for long pulses and high fluences is one bottleneck of the plasma mirror concept. We will see in Sec. V what ranges of pulse duration and fluence should be used to avoid this kind of distortion.

IV. MODELING OF THE PLASMA MIRROR

In this section, we describe the two models that we have used to describe (1) the optical switching of the PM and (2) its expansion into vacuum.

The first model (''population-propagation model'') describes the ionization of the target (in this case, bulk quartz) with a population equation, and the propagation of the laser field in this inhomogeneously ionized medium, using the Helmholtz wave equation. This model is very simple, but captures the essential physics of the plasma mirror. The second model is a hydrodynamic model based on a Lagrangian fluid code, and is required to describe the regime where the hydrodynamics must be included because the plasma expands into vacuum. The equations describing the ionization of the target and the propagation of the field are equivalent in these two models.

In all these simulations, it is assumed that the pedestal and the prepulses do not affect the target. This can be considered as a prerequisite to make a good plasma mirror (see Sec. V), and, knowing the contrast of the LUCA laser, is a reasonable assumption for the experiments presented in this paper (see Sec. II).

A. The population-propagation model

We consider a plane wave coming from vacuum impinging on the target. The target is initially a pure dielectric, with no electron in the conduction band. Our goal is to calculate the electric field $E(z,t)$ inside the target, taking into account the fact that the target gets ionized by this strong field. Once $E(z,t)$ is known, the reflectivity of the plasma can readily be calculated (see the Appendix).

To describe the field propagation, we use the quasistationary approximation, which consists in considering that the electric field at any point is harmonic in time, at the frequency of the external driving field. It is valid only if the temporal evolution of the dielectric function is slow on the time scale of the incident laser pulse optical cycle. If this is not the case, more sophisticated approaches are required [27].

Assuming that we are in this quasistationary regime, the propagation of an *S*-polarized electromagnetic wave, impinging on a medium defined by its dielectric function $\varepsilon(z,t)$ (with $z>0$), with an angle θ, is described by the Helmholtz equation [19]

$$\frac{\partial^2 E(z,t)}{\partial z^2}+\frac{\omega^2}{c^2}[\varepsilon(z,t)-\sin^2(\theta)]E(z,t)=0, \qquad (1)$$

where ω is the angular frequency of the incident pulse, and c is the speed of light in vacuum. $\epsilon(z,t)$ is the dielectric function of the plasma and is given by the Drude model:

$$\varepsilon(z,t)=n_1^2-\frac{e^2N(z,t)}{\epsilon_0 m^*(\omega^2-i\omega/\tau)}. \quad (2)$$

n_1 is the initial refractive index of the solid, e is the electron charge, m^* its effective mass, and ϵ_0 is the vacuum permittivity. τ is the mean electron collision time, and is assumed to be a constant (e.g., independent of the electronic temperature) in this model. We will see that this approximation is satisfactory up to a certain fluence, above which the plasma gets too hot and expands too much during the laser pulse to consider τ as a constant. $N(z,t)$ is the instantaneous conduction electron density at point z. Its varies in time because of the nonlinear excitation of the dielectric by the high-intensity incident laser pulse. This in turn results in a time dependence of the dielectric constant $\epsilon(z,t)$. $N(z,t)$ also depends on z because once some electrons are in the conduction band, they can absorb some energy from the incident field since the collision time $\tau\neq 0$. The laser field in the dielectric thus becomes inhomogeneous, and so is the excitation density.

Before the main laser pulse, the conduction electron density is assumed to be zero: $N(z,t=0)=0$. Its temporal evolution is then given by a rate equation:

$$\frac{\partial N}{\partial t}=W(N_0-N), \quad (3)$$

where W is the electron excitation rate from the valence band to the conduction band, and N_0 is the bound electron density. We have considered that the excitation is both due to multiphoton absorption and electronic avalanche [21,22], with W given by

$$W=\sigma_n|E(z,t)|^{2n}+\beta\frac{N}{N_0}|E(z,t)|^2. \quad (4)$$

n is the minimum number of photons required to cross the band gap and σ_n is the corresponding cross section. A band gap of about 10 eV for quartz and a photon energy of 1.57 eV leads to $n=6$. Using a tunneling excitation law instead of a multiphotonic mechanism gives very close results [28].

The technique used to solve the coupled system of equations (1) and (3) is described in the Appendix A.

Figure 9 shows the instantaneous conduction electron density $N(z,t)$ in the target, obtained with this model, as a function of z, for various times in the rising edge of a 50 J/cm^2 pulse. The laser pulse duration is 60 fs, but these profiles vary very little with the pulse duration within this model. At early times, the absorption of the laser beam is weak and therefore the target is homogeneously excited on a micron length scale. As intensity increases, the excitation of the target gets higher. This implies that the laser pulse gets attenuated as it penetrates in the target, which leads to an inhomogeneous excitation. When the critical density is overcome, this inhomogeneity gets even stronger, since the laser field does not penetrate further than the skin depth. As can be seen in Fig. 9, at the maximum of the pulse, the excitation density near the surface varies by two orders of magnitude over a distance of about 200 nm only, i.e., smaller than the wavelength of the incident radiation. This is why the WKB approximation or the Fresnel equation cannot be used to calculate the field propagation in the target and the reflection coefficient: to evaluate these quantities properly, the Helmholtz equation has to be solved [19].

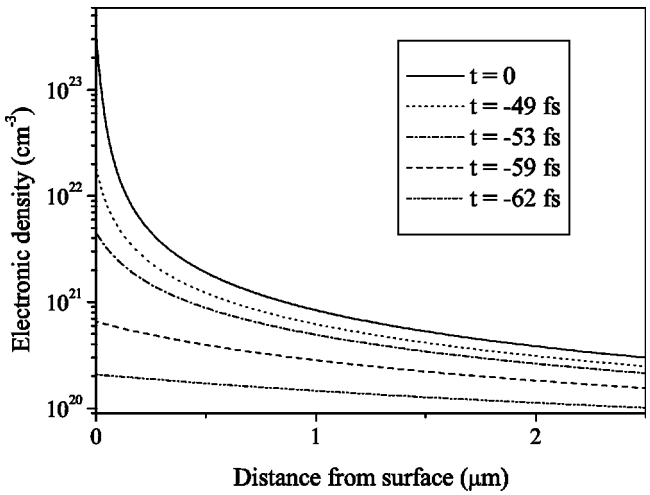

FIG. 9. Spatial profile of the instantaneous conduction electron density $N(z,t)$ in the target, along the beam propagation direction z, at different times in the rising edge of a 50 J/cm^2, 60 fs pulse. $t=0$ corresponds to the peak of the pulse.

Figures 2 and 3 compare the measured fluence dependences of the peak and overall reflectivities with the ones calculated with this model, for a 60 fs laser pulse. Figure 4 shows the same comparison for the overall reflectivity of a 4 ps pulse. The set of parameters used for these calculations is shown in Table I. In all cases, the agreement is very satisfactory. This shows that this simple model, with the set of parameters given in Table I, is adequate to calculate the reflectivity of the PM in a broad range of pulse duration and fluence.

We note that the avalanche coefficient β we have obtained (Table I) is the same as the one deduced from optical breakdown threshold measurements in silica [21,22]. The mean electron collision time τ is in reasonable agreement with the hot electron-acoustic phonon collision times in wide band-gap dielectrics [29,30]. It also has the typical order of magnitude of electron-ion collision times in near-solid-density plasmas at electronic temperatures between 10 and 100 eV [31]. An electron density of 5×10^{23} cm^{-3} approximately corresponds to what would be obtained by ionizing all the electrons except the $1s$ and $2s$ of Si and the $1s$ of O. Given the ionization potentials of these states (>500 eV), this is a realistic value for N_0. The electron effective mass m^* had little influence on the results of the simulations within this model, and was taken to be the free electron mass.

TABLE I. Set of parameters used in the population-propagation model to fit the reflectivity curves of Figs. 2–4.

σ_6 (cm^{12} s^5)	β(cm^2/J)	τ(fs)	N_0 (cm^{-3})
2.3×10^{-178}	11	0.1	5×10^{23}

B. The hydrodynamic model

In order to describe the PM response in the high-intensity regime or for longer interaction times, we need a hydrodynamic simulation, which describes the plasma expansion, and accounts for multionized atomic states and collisional processes in the high temperature plasma. We use FILM, a standard one-dimensional Lagrangian fluid code [20,32]. This code solves fluid equations associated with conservation of energy, momentum, and mass. The electronic thermal conductivity is also included in this code. To close the system of hydrodynamic equations, an equation of state derived from the SESAME library [33] is used. This equation of state provides the temperature, pressure, mean ionization (Z) and electron density for each internal energy and mass density. Knowing the temperature and density, the elastic electron-ion collision frequency is deduced from the model of Lee and More [31], which converges to the Spitzer results for high temperatures [34]. To compute the energy source due to the laser field, the Helmholtz equation is solved as in the simple model previously described, now taking into account the electron-ion collisions to calculate the collision rate.

FILM is not suited to describe the first stage of the excitation, where the mean ionization is low and the target is closer to a solid than to a plasma. We have modified the code to describe this stage and the transition to a plasma. Thus, for $Z<1$, we are using a modified equation of state: in this regime, the internal energy is assumed to be equal to the electron density multiplied by the band-gap energy plus an effective electron thermal energy. This last contribution is a small fraction of the band gap. To account for multiphoton ionization (not included in FILM), which is the dominant process at low electron density, multiphoton absorption is included as an energy source in the energy equation. The electron-phonon collision frequency is used in the Drude equation (2), to calculate the dielectric constant (and therefore the field and the collisional absorption). In order to get a soft transition between the high and low excitation density regimes, the two equations of state are interpolated for $1<Z<2$ and the electron-phonon collision frequency is assumed to be proportional to $(1-Z)$, for $Z<1$. Numerical tests show that the results are insensitive to the details of the interpolation.

The upper graph in Fig. 10 shows the instantaneous reflectivity at time t obtained from this model, as a function of the total energy that has impinged on the target up to time t, for three pulse durations. Since fluence is the relevant physical parameter for the PM, this x scale is well suited to compare the temporal evolutions obtained for a wide range of incident pulse duration. The lower graph shows the corresponding plasma temperatures. Since we are interested in the effects on the reflectivity, these temperatures were taken at the point where the electronic density is equal to the critical density. Once the plasma mirror has triggered, temperatures typically between 10 and 100 eV are reached in the plasma.

In all cases, a rapid increase of the reflectivity is observed when the critical density is overcome, followed by a plateau. This plateau corresponds to a reflectivity of $\approx 65\%$ only,

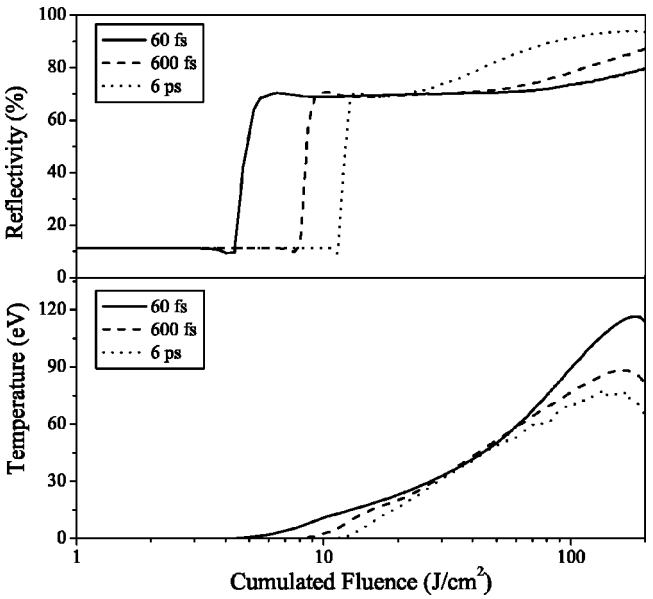

FIG. 10. Upper graph: instantaneous reflectivity as a function of the cumulated fluence for several pulse durations, as obtained from the hydrodynamic model. The total fluence of the incident pulse is 200 J/cm^2 in all cases. Lower graph: corresponding plasma temperatures at the critical density.

because of the high collision rate ($1/\tau \approx 10$ fs^{-1}) in the plasma. This fast increase of the reflectivity and the following plateau imply that the PM acts almost like a high-pass filter with respect to fluence: in a certain fluence range above the triggering threshold, the laser field is reflected with an almost constant reflectivity. The advantages of this feature will appear in the following discussion (Sec. V). The fast increase of the instantaneous reflectivity seen in Fig. 10 is not in contradiction with the smooth dependence of the reflectivity measured experimentally (Figs. 2–4): this smooth dependence is essentially due to the triggering of the PM at earlier times and over larger areas as the incident fluence increases.

In the case of the 60 fs pulse, the reflectivity starts to increase again in the second-half of the pulse (cumulated fluence >100 J/cm^2): this is due to the increase of the electron temperature (see lower graph), which leads to a reduction of the electron-ion collision rate. For ps pulses, the reflectivity increase occurs at lower fluences, corresponding to lower temperatures: in this case, it is mostly due to the expansion of the plasma during the laser pulse, which leads to a decrease of the plasma density and hence of the electron-ion collision rate.

The population-propagation model described previously gives very similar curves, except for the late increase in reflectivity, which can obviously not be described by this simple model.

Figure 8 compares the measured temporal evolution of the reflected beam phase at different fluences with the results obtained with this model. A very good agreement is obtained at all fluences without changing any parameter in the calculation. This model can therefore be used to calculate the phase shift induced by the PM on the reflected beam. As

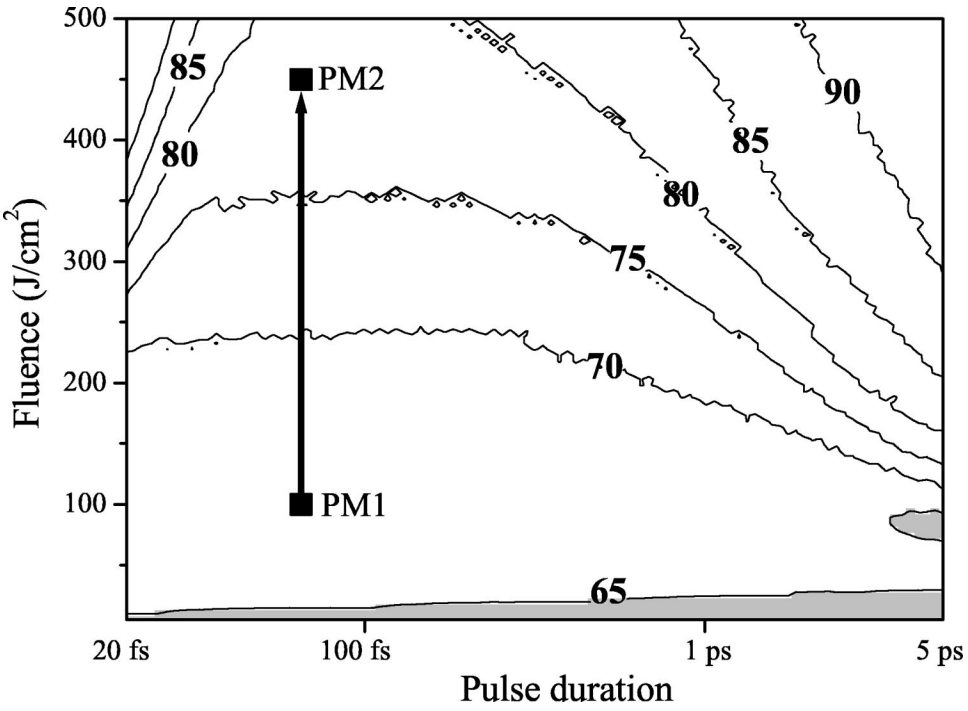

FIG. 11. Reflectivity of the PM at the maximum of the laser pulse, as a function of the duration and fluence of the incident pulse. The area where the PM can be considered to trigger (reflectivity $>65\%$) appears in white. The two points PM1 and PM2 show the typical fluences that could be used in a two-PM system, allowing contrast improvements by several 10^4.

mentioned earlier, it shows that this phase shift originates mostly from the motion of the critical density surface due to the plasma expansion in vacuum. The curves in Fig. 8 show that the plasma only starts to expand after a time t_e, which not surprisingly decreases as the incident fluence increases. After time t_e, it expands with a constant velocity, which is found to be 3×10^7 cm/s for a fluence of 50 J/cm^2, in good agreement with previous experiments [35].

V. DISCUSSION

Our models have been validated by comparison with our experimental data: we can now use them to assess the performances of the PM, and determine its optimal operational fluence as a function of the incident pulse duration.

This optimal fluence is determined by a trade-off between the following constraints: (1) the reflectivity of the PM should be as high as possible at the maximum of the laser pulse; (2) the PM should not distort the beam wave front too much; (3) for an optimal improvement of the contrast, the PM should trigger only in the rising edge of the main pulse. If the triggering does not occur too early in the rising edge, a steepening of this edge can even be induced by the PM (see Fig. 6), which can be highly desirable for some experiments.

Given these constraints, the optimal fluence can be chosen with the help of Figs. 11 and 12, obtained with the models previously described. These figures, respectively, show the reflectivity R of the PM at the spatial and temporal maximum of the laser pulse, and the phase shift it induces at the end of the laser pulse, as a function of the duration and fluence of the incident pulse. In Fig. 11, the gray area indicates the range of parameters where the PM does not trigger. This area was arbitrarily defined by the threshold $R<65\%$. The exact value chosen for this threshold does not matter because the reflectivity varies very strongly with the fluence when $R \lesssim 65\%$. The triggering fluence threshold is almost independent of the pulse duration, as observed experimentally. The gray area on the phase map (Fig. 12) corresponds to an induced phase shift higher than 1 rad ($\approx\lambda/6$), i.e., to a significant distortion of the beam wave front (since this phase shift goes to 0 on the edges of the beam).

Several regimes can be distinguished on the reflectivity map. For pulses shorter than ≈600 fs and fluences between the triggering threshold and ≈300–500 J/cm^2 (depending on the pulse duration), the reflectivity is remarkably insensitive to the fluence, and is $\approx70\%$. This weak dependence is due to the fact that in this range (1) the plasma is extremely overdense whatever the fluence, (2) the collision rate hardly varies with temperature ($T\approx10$–100 eV) [31] and hence with fluence, and (3) the pulse is short enough to neglect the plasma expansion (see Fig. 12). In this regime, the PM is very robust against shot-to-shot fluctuations and spatial inhomogeneities of the fluence, at the expense of an energy loss of $\approx30\%$ at the peak of the pulse. In the same duration range, higher efficiencies of $\approx85\%$ can be obtained by using higher incident fluences, at the expense of robustness: the PM then enters a new regime, where the reflectivity again increases with the fluence, because of the heating of the plasma and the resulting decrease of the collision rate. Figure 12 shows that in this short pulse duration range, the PM hardly induces any distortion of the beam wave front even at the highest fluences considered here, because the plasma does not have time to expand during the main laser pulse.

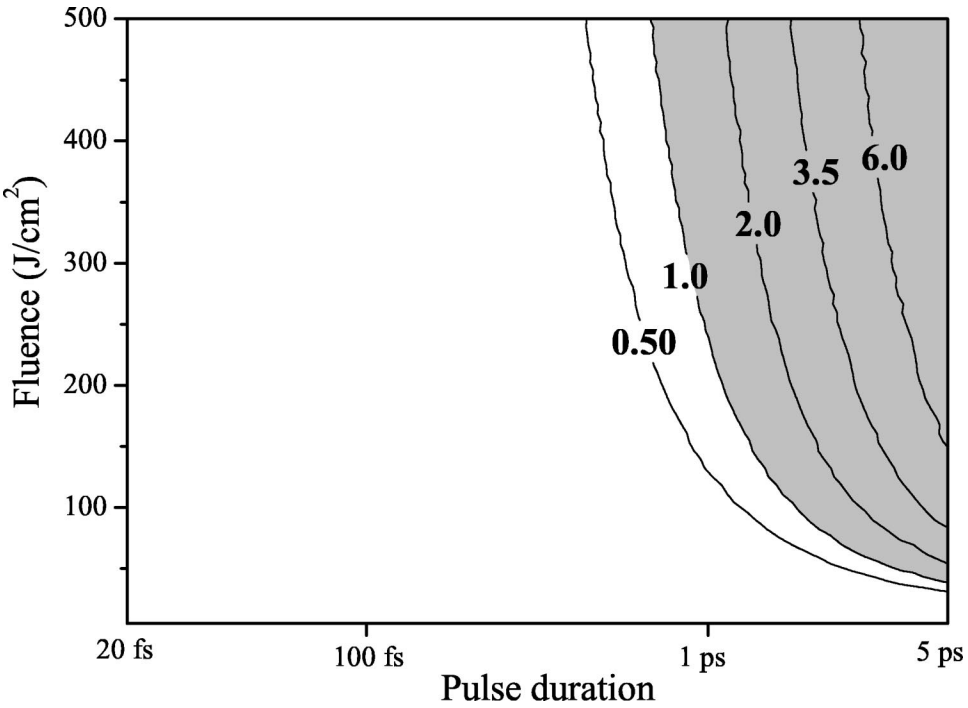

FIG. 12. Phase shift of the reflected field at the end of the laser pulse (1.5 FWHM after the maximum of the pulse), as a function of the duration and fluence of the incident pulse. In the gray area, the PM induces a significant distortion (>1 rad) of the beam wave front.

For pulses longer than ≈ 1 ps, the robust reflectivity regime shrinks. Higher reflectivities can be reached at lower fluences because the plasma expansion has already started at the maximum of the pulse. However, the PM is less robust against fluence variations since the fluence dependence of the reflectivity is stronger. Moreover, the operational fluence range (between the gray area in Fig. 11 and the one in Fig. 12) is of course reduced because of this expansion. For pulses longer than ≈ 5 ps, the PM becomes inadequate since a distortion of the wave front cannot be avoided as soon as the PM triggers.

These two maps can be used to design a PM system suited to a particular high-power laser system, provided the initial temporal contrast of the laser is known. This last information is required to ensure that the PM triggers only in the rising edge of the main pulse: the initial contrast determines the maximum main pulse fluence that can be used on the PM. For fluences higher than this limit, the pedestal or prepulses will trigger the PM. In this case, the contrast improvement will not be optimal, and a strong distortion of the main beam wave front might be induced because of the longer time available for the plasma to expand. With typical contrast of 10^6 on a ns time scale and 10^4 on a ps time scale, this maximum fluence will typically be of the order of 100 J/cm^2 (point PM1 in Fig. 11). As we have seen, an antireflection coated PM used at this fluence leads to an improvement of the contrast by a few 10^2. Depending on the initial contrast, this might not be enough for some high-field experiments, and a second PM might be required to increase the contrast even more [5]. This second mirror can be used at a higher fluence (point PM2 in Fig. 11), since it is triggered by a pulse with a higher contrast. Such a system with two PMs made of antireflection coated plates can lead to an improvement of the contrast by several 10^4.

These two PMs can be implemented in several ways for an actual high-field experiment.

One possibility is to insert them between the target and the short focal length optics used to focus the beam on the target. Such a setup is compact, but is not very flexible and can be challenging to implement. The PMs act in the intermediate field: to avoid severe distortions of the focal spot, one has to be especially careful with the phase and amplitude distortions they might induce. This implies that both PMs should be used in the white area of the phase map, and in the robust regime, where the reflectivity weakly depends on the fluence.

Another possibility is to implement the PMs before the optics that focuses the beam on the target, by inserting them in a long focal length $2f$ line (such as in a spatial filter). The first PM would be located before the focal point of this spatial filter, while the second one would be at the focus. The constraints on the phase and amplitude distortions induced by the second PM are then less severe, since the beam reflected from this mirror will be imaged on the target. Like in our experiment (see Sec. III B), this PM would both act as a temporal and a spatial filter. If the phase distortion induced by this mirror really gets strong, a part of the beam might not be collected by the second optics of the $2f$ line, which would lead to energy losses.

VI. CONCLUSION

We have carried out a detailed experimental study of a plasma mirror temporal filter, aimed at improving the tempo-

ral contrast of high-power ultrashort laser pulses. Besides standard reflectivity measurements, an original method [25] based on the use of chirped laser pulses has allowed us to identify, in a single shot and on a ps time scale, the stages of the construction of a plasma mirror, from the ionization of the target to the plasma expansion in vacuum. This expansion in vacuum has very important practical consequences, since it might lead to distortions of the reflected beam wave front and prevent a good subsequent focusing. Our diagnostic is thus particularly relevant to determine the upper fluence limit for the plasma mirror to work properly.

We have used our experimental results as an accurate benchmark test to validate numerical models of the plasma mirror. These models can then be used to find the optimal working conditions for the plasma mirror, for fs to ps pulses. An essential result of this theoretical study is that the peak plasma mirror reflectivity is hardly influenced by the incident fluence between a few J/cm^2 and a few hundreds of J/cm^2, for pulse durations ranging from a few tens to several hundreds of fs. The plasma mirror is thus very robust against shot-to-shot energy fluctuations, and does not accentuate the possible spatial inhomogeneities of the laser beam. The longest pulse duration that can be handled with a plasma mirror was found to be about 5 ps: beyond this duration, severe distortions of the beam wave front due to the plasma expansion become unavoidable.

Lastly, our measurements have shown that using an antireflection coated dielectric as a target makes it possible to increase the temporal contrast by several 10^2 with a single plasma mirror. Using two plasma mirrors in series should lead to temporal contrasts as high as 10^{10}–10^{11} on a ns time scale, and 10^7–10^8 on a ps time scale. Such contrasts open the route to a whole range of new ultrahigh intensity experiments.

ACKNOWLEDGMENTS

This work was done under the hospice of the SHARP Contract No. HPRI-CT-2001-50037. P. d'Oliveira and P. Monot are strongly acknowledged for helpful discussions.

APPENDIX

In this appendix, we explain how to solve numerically the coupled equations (1) and (3), and we more particularly specify how to deal with the initial conditions on the electric field $E(z,t)$.

When a plane wave impinges (with an incidence angle taken to be 0 for simplicity) on a medium with a dielectric constant $\epsilon(z)$, a part of the field energy, given by the complex reflection coefficient r, will be reflected back in vacuum ($z<0$), and thus produce standing waves on the vacuum side by interference with the incident beam. The continuity of the electric field and its z derivative at the vacuum-target boundary leads to

$$E_0(1+r)=E(z=0^+), \tag{A1a}$$

$$ik_0E_0(1-r)=\frac{dE}{dz}(z=0^+). \tag{A1b}$$

E_0 is the amplitude of the incoming electric field, and $k_0=\omega/c$. For a strongly inhomogeneous medium such as the plasma mirror (see Fig. 9), the reflection coefficient r cannot be simply obtained from the Fresnel equations, and is therefore unknown. As a result, $E(z=0^+)$ and $dE/dz(z=0^+)$ cannot be calculated from Eqs. (A1), and we have no initial condition to solve the Helmholtz equation (1) in the $z>0$ area.

A solution to this problem consists in solving the Helmholtz equation backward, i.e., from a region far inside the target, where the refractive index is constant in space, to the target surface. We then need an initial condition at a point $z=L$ in this region. Since the medium is almost homogeneous around this point, we know that the electric field is a plane wave propagating in the positive direction of the z axis. Only the magnitude A of this wave is unknown. We define $\psi(z,t)$ by $E(z,t)=A\psi(z,t)$ and $|\psi(z=L)|=1$. The initial conditions on $\psi(z)$ at $z=L$ will thus be

$$\psi(z=L)=\exp(ik_1L), \tag{A2a}$$

$$\psi'(z=L)=ik_1\exp(ik_1L) \tag{A2b}$$

with $\psi'(z)=d\psi/dz$ and $k_1=n_1\omega/c$. Moreover, $\psi(z)$ also obeys the Helmholtz equation since this equation is linear. $\psi(z)$ is thus calculated by solving the Helmholtz equation from $z=L$ to $z=0$. Once $\psi(z)$ is known, Eqs. (A1) can be combined to obtain the reflection coefficient

$$r=\frac{ik_0\psi(z=0)-\psi'(z=0)}{ik_0\psi(z=0)+\psi'(z=0)}. \tag{A3}$$

The actual electric field $E(z,t)$ can then be deduced from $\psi(z,t)$ and the known amplitude of the incident electric field at the surface, using

$$A=E_0\frac{1+r}{\psi(z=0)}. \tag{A4}$$

The electric field is now completely determined at time t. We use its value to calculate the ionization rate W, and the excitation density $N(z)$ at time $t+dt$. Knowing $N(z,t+dt)$ we calculate the dielectric function using Eq. (2). $\epsilon(z,t+dt)$ can then be used in the Helmholtz equation (1), to determine electric field at time $t+dt$.

[1] J.D. Bonlie *et al.*, Appl. Phys. B: Lasers Opt. **70**, S155 (2000).
[2] D. Umstadter, Phys. Plasmas **8**, 1774 (2001).
[3] D. Strickland and G. Mourou, Opt. Commun. **56**, 219 (1985).
[4] V. Bagnoud and F. Salin, IEEE J. Sel. Top. Quantum Electron. **4**, 445 (1998).
[5] I. Watts *et al.*, Phys. Rev. E **66**, 036409 (2002).

[6] F. Brunel, Phys. Rev. Lett. **59**, 52 (1987).
[7] M. Grimes, A. Rundquist, Y. Lee, and M. Downer, Phys. Rev. Lett. **82**, 4010 (1999).
[8] M. Nantel *et al.*, IEEE J. Sel. Top. Quantum Electron. **4**, 449 (1998).
[9] J. Itatani *et al.*, Opt. Commun. **148**, 70 (1998).
[10] G. Chériaux *et al.*, Conference on Lasers and Electro-Optics, Postconference Technical Digest, 45 (2001).
[11] I. Jovanovic *et al.*, Appl. Opt. **41**, 2923 (2002).
[12] H.C. Kapteyn, M. Murnane, A. Skoze, and R.W. Falcone, Opt. Lett. **16**, 490 (1991).
[13] D.M. Gold, H. Nathel, P.R. Bolton, W.E. White, and L.D.V. Woerkom, Proc. SPIE **1413**, 41 (1991).
[14] S. Backus *et al.*, Opt. Lett. **18**, 134 (1993).
[15] D.M. Gold, Opt. Lett. **19**, 2006 (1994).
[16] Z. Bor *et al.*, Appl. Phys. A: Mater. Sci. Process. **60**, 365 (1995).
[17] C. Ziener *et al.*, J. Appl. Phys. **A93**, 768 (2003).
[18] J. Freidberg *et al.*, Phys. Rev. Lett. **28**, 795 (1971).
[19] W.L. Kruer, *The Physics of Laser Plasma Interactions* (Addison-Wesley, Reading, MA, 1988).
[20] J.-C. Gauthier, J.-P. Geindre, N. Grandjouan, and J. Virmont, J. Phys. D **15**, 32 (1983).
[21] B. Stuart *et al.*, Phys. Rev. Lett. **74**, 2248 (1995).
[22] B. Stuart *et al.*, Phys. Rev. B **55**, 5799 (1997).
[23] M. Takeda, H. Ina, and S.J. Kobayashi, J. Opt. Soc. Am. **72**, 156 (1982).
[24] A. Benuzzi-Mounaix *et al.*, Phys. Rev. E **60**, R2488 (1999).
[25] J.-P. Geindre, P. Audebert, S. Rebibo, and J.-C. Gauthier, Opt. Lett. **26**, 1612 (2001).
[26] F. Quéré *et al.*, Europhys. Lett. **56**, 138 (2001).
[27] M. Geissler *et al.*, Phys. Rev. Lett. **83**, 2930 (1999).
[28] E.J. Jarque, V. Malyshev, and L. Roso, J. Mod. Opt. **44**, 563 (1997).
[29] M. Fischetti *et al.*, Phys. Rev. B **31**, 8124 (1985).
[30] E. Cartier and F.R. McFeely, Phys. Rev. B **44**, 10 689 (1991).
[31] Y.T. Lee and R.M. More, Phys. Fluids **27**, 1273 (1984).
[32] J.F. Luciani, P. Mora, and J. Virmont, Phys. Rev. Lett. **116**, 237 (1986).
[33] Los Alamos National Laboratory, Technical Report No. LA-UR-92-3407, edited by S.P. Lyon and J.D. Johnson, 1992 (unpublished).
[34] L. Spitzer, *Physics of Fully Ionized Gases*, 2nd ed. (Interscience, New York, 1962).
[35] B.T.V. Vu, A. Szoke, and O.L. Landen, Phys. Rev. Lett. **72**, 3823 (1994).